NANO LETTERS

2008
Vol. 8, No. 8
2258-2264

Polarization Driven Covalently-Bonded Octahedral-Twinning and Backbone-Peripheral-Helical Nanoarchitectures

Xiaodong Han,*,† Shanliang Zheng,† Yuefei Zhang,† Kun Zheng,† Shengbai Zhang,*,‡ Ze Zhang,*,† Xiaona Zhang,† Xianqiang Liu,† Gang Chen,† Yajuan Hao,§ and Xiangyun Guo§

Institute of Microstructure and Property of Advanced Materials, Beijing University of Technology, Beijing, 100124, China, Department of Physics, Applied Physics, and Astronomy, Rensselaer Polytechnic Institute, Troy, New York 12180, and Key Laboratory of Coal Conversion, Institute of Coal Chemistry, Chinese Academy of Sciences, Taiyuan 030001, China

Received March 27, 2008

ABSTRACT

We report the novel superstructural chiral polar-surface induced backbone-peripheral-helical (BPH) hierarchical architecture of zincblende SiC made possible by precise helical epitaxy. We show by direct image that this architecture has the mother−daughter relationship. The center of the BPH consists of periodic octahedral modular units with chiral sidewalls. By forming Si−C covalent bonds at the sidewalls, a daughter SiC wire spontaneously vine-grows in a peripherally helical way on the mother wire. All of the information of the mother wire, including twinning, polarity and even stacking fault, are completely copied and inherited by the daughter wire one-by-one at the atomic level. Our findings thus provide a simple growth method and the necessary atomistic mechanism for novel polar surface driven superstructural twinning and subsequent BPH growth, which should be universal for zincblende semiconductors and even could be true for other noncentral-symmetric compounds.

From seashells to DNA,[1–3] backbone-peripheral-helical (BPH) structure is ubiquitous in nature. It is also a necessary element in liquid crystals[4,5] and supra-molecule polymers.[6,7] Through spontaneous self-assembly of the various chemical elements and structural units at multilength scales (atomic, molecular, and supra-molecular) by noncovalent interactions such as hydrogen bond and electrostatic interactions,[8,9] the sophisticated backbone superstructure dictates the formation of the more complex BPH hierarchical architecture in aqueous media.[10,11] For one-dimensional inorganic nanomaterials,[12–15] free-standing nanohelical wires have been synthesized for carbon nanotubes,[16] SiC,[17] amorphous SiC,[18] GaAs,[19] ZnO,[20–23] SiO_2,[24] GaN,[25a] $ZnGe_2O_4$,[25b,26] Zn_2SnO_4,[25b] SiGe/Si,[27] and Si[28] through pentagon-heptagon carbon rings,[16] screw dislocations,[17] unsymmetrical catalysis,[18,19] and the spontaneous polarization.[20–23] The zigzag one-dimensional nanomaterials were reported to be popular in zincblende structural materials. However, BPH architecture which consists of these two components has not been synthesized in solid−vapor media or covalently bonded semiconductors. Here, we report the novel superstructural chiral polar-surface induced BPH hierarchical architecture of zincblende SiC made by precise helical epitaxy. The center of the BPH consists of periodic octahedral modular units with chiral sidewalls. Our findings provide a simple growth method and the necessary atomistic mechanism for novel polar surface driven superstructural twinning[29–32] and subsequent BPH growth. The results thus provide a possible universal rule for zincblende semiconductors and even could be true for other noncentral-symmetric compounds which are important for controlling the morphology and the quality of these one-dimensional nanomaterials.

The synthesis process of SiC NWs includes the xerogel preparation and a subsequent carbon-thermal reduction which was similar to the process in ref 33. The as-prepared xerogel was heated in Ar flow (60 cm^3/min) to 1050 °C at a rate of 10 °C/min, then to 1350 °C at a rate of 2 °C/min and maintained at this temperature for 6 h. The raw product was

* Corresponding author. E-mail: xdhan@bjut.edu.cn (X.H.), zezhang@bjut.edu.cn (Z.Z.), and zhangshengbai@gmails.com (S.Z.).
† Beijing University of Technology.
‡ Rensselaer Polytechnic Institute.
§ Chinese Academy of Sciences.

10.1021/nl080880w CCC: $40.75
Published on Web 07/11/2008

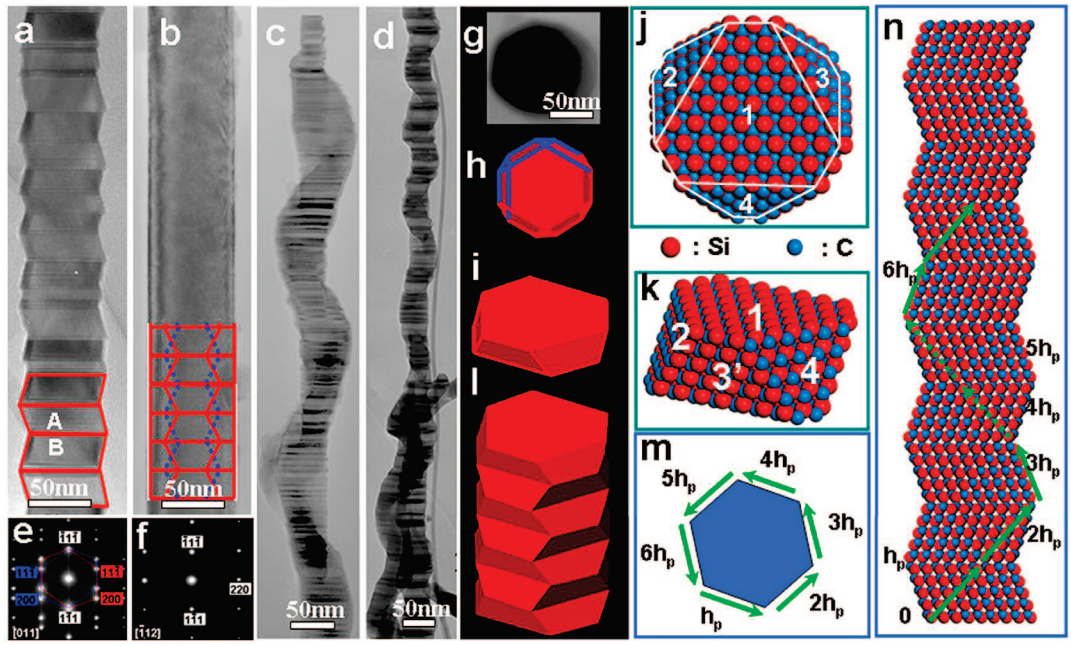

Figure 1. Morphology and structure of the SiC octahedral twinning nanowire backbones and the backbone-peripheral-helical NWs. (a−d) TEM images of the SiC nanowires: zigzag pillars viewed along (a) [011] and (b) [−112]. (c) Right-handed and (d) left-handed BPH. (e,f) SAEDPs corresponding to (a,b). (g) Top view of the zigzag pillar. (h,i) Top and perspective view of a modular unit of the pillar. (j,k) Same as (h,i) but in an atomistic structural model. Indexes 1, 2, 3(3′), and 4 indicate four nonorthogonal {111} surfaces. (l) Pillar as a result of modular units in (i) stacking along [1−11]. (m,n) Top and [011] side view of the twinning derived rotational chirality. Green arrows indicate the direction of rotation. After each rotation, the height of the pillar increases by h_p (h_p is the fully grown height of the octahedral unit), and upon 6 consecutive rotations, 1 cycle is completed. The red lines in (a) and (b) frame the edge trace of the octahedral pillar at the front side, and the blue lines in (b) draw the edges of the octahedron at the back-side.

heated in air at 700 °C for 4 h to remove the residual carbon, and subsequently treated by nitric acid (HNO_3) and then hydrofluoric acid (HF) to eliminate the residual silica and other impurities.

The product was examined by field emission gun scanning electron microscopy (SEM; JEOL JSM-6500F) with a 30 KV and beam current of 5 nA. A small piece of the as-synthesized product was dispersed ultrasonically for 15 min in ethyl alcohol and placed on a Cu supporting carbon microgrid for immediate transmission electron microscopy (TEM) examination. Conventional TEM analysis and high resolution (HR)-TEM were conducted using a JEOL-2010F with a point resolution of 0.19 nm, and it was operated at 200 kV. Morphology observation and selected area electron diffraction pattern (SAEDP) as well as atomic scale observations of the samples were conducted. The atomic model of SiC is set up with the commercialized software CrystalKit and the HRTEM simulation was carried out with Mactempas. Multislice approximation method was used in simulating the HRTEM images. The simulation parameters were chosen to be close to the experimental ones. Convergent-beam electron diffraction (CBED) was conducted using a spot size of 5 nm. The polarities of the SiC were identified by CBED through comparing the experimental and the Bloch simulated[34] results. The simulated patterns were with 160 nm in thickness and 32 beams included.

The synthesis of the BPH nanowire pairs (NWPs) includes the xerogel preparation and a subsequent carbon-thermal reduction.[33] Both freestanding SiC zigzag nanowire pillars (Figure 1a,b) and BPH NWPs (Figures 1c,d) were observed by the TEM. The BPH NWP consists of a central backbone and a peripheral helical wire. The backbone has identical structure with that of the freestanding zigzag pillar. The peripheral helical wire has well-developed helical structure, relatively uniform diameter, repeatable helical pitch, and well-defined helical angle: among more than 50 BPH NWPs, the diameters range from 20 to 90 nm; the pitch distances range from 150 to 200 nm with lengths ranging from 100 to 200 μm, and two characteristic projected helical angles of 62° along ξ and 58.5° along λ. Both left- and right-handed helical structures were observed, as shown in Figure 1c,d with a ratio close to one. The statistics of BPH nanowire pairs has been shown in Figure 2. The as-synthesized SiC samples contain about 10−20% of the BPH NWPs (Figure S1, Supporting Information).

As the freestanding zigzag pillar holds the key to BPH formation, it is essential to first understand its structure. The zigzag pillar is shown in Figure 1a (viewed along [011]) and Figure 1b (viewed along [−112]). The pillar in Figure 1a is marked by two nanofacets A and B, respectively, separated by a twin boundary. SAEDP in Figure 1e also reveals such a twinning, so the two facets A and B can be indexed as two different {111} planes. CBED were taken from A and B respectively and then simulated (Figure S2, Supporting Information). The simulated (002) and (00−2) diffraction disks agree well with the experiment and indicate an ortho-twin feature (Figure S2). There are three equivalent ξ viewing directions. Therefore, there are three sets of {111} facets like the one in Figure 1a. In other words, each segment of the zigzag pillar consists of 6 truncated {111} facets. When rotating along the longitudinal direction by 30° toward

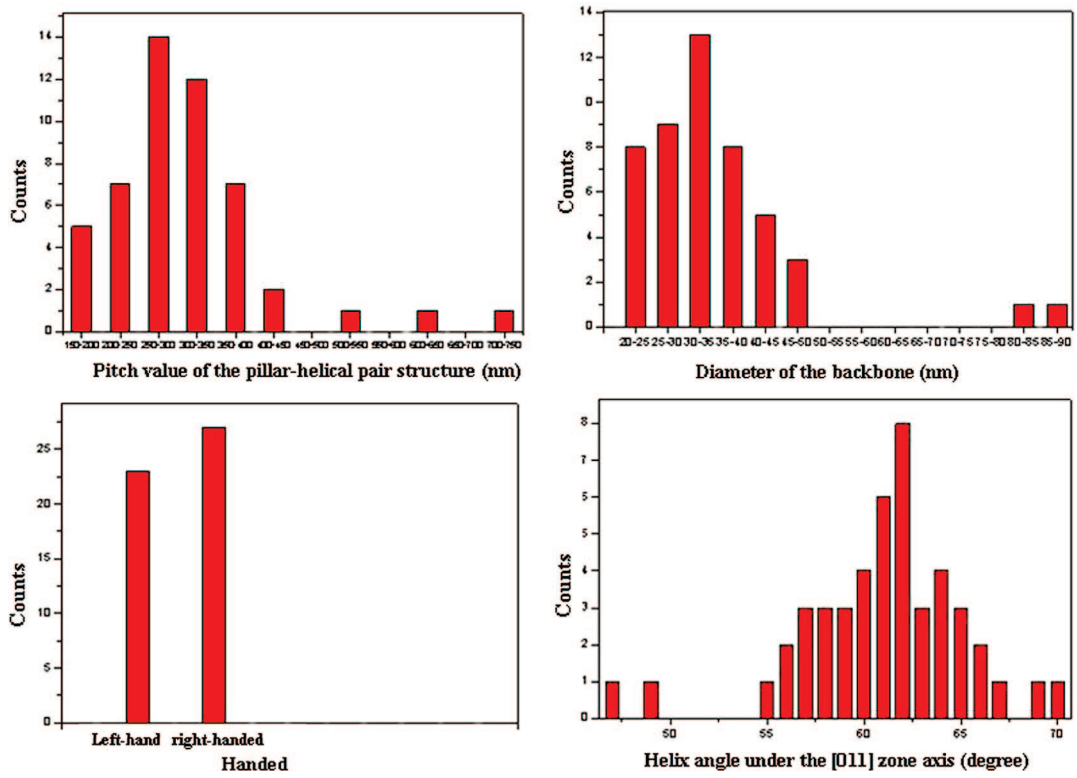

Figure 2. Statistics of the observed SiC backbone-peripheral-helical nanowire pairs where (a) is the pitch values and (b) is the diameter of the backbone pillar, (c) is the handedness, and (d) is the projected helical angle under [011] zone axis observation.

[−112] (Figure 1b), however, such zigzag feature can no longer be seen, and the corresponding SAEDP in Figure 1f is that of a single crystal. The cross-sectional TEM image in Figure 1g shows indeed a typical hexagonal shape, as schematically depicted in Figure 1h, from which we deduce the basic modular unit of the pillar (Figure 1i) as a truncated {111} octahedron with 6 {111} sidewalls and 2 {111} surfaces in the longitudinal direction. The octahedron has 4 equivalent polarization directions, 1, 2, 3, and 4 in Figure 1j,k. Stacking of the modular units yields the zigzag pillar in Figure 1l. Figure 1m,n shows that the 60° consecutive twinning naturally derives chirality. Next, we characterize the BPH NWPs. Low magnification TEM images in Figure 3a reveal the hybrid characters of the BPH architecture. Enlarged dark field image in Figure 3b shows identical contrast of the helical wire with that of the pillar wire, indicating structural and orientation uniformity across the boundary. The electron diffraction pattern in Figure 3c, taken from a single period of the BPH NWP, shows a typical face centered cubic (FCC) {111} twinning. Figure 3a−c thus reveals clearly the epitaxial nature of the helical NW grown on top of the pillar NW. Figure 3d is an HRTEM image of the interfacial structure for the BPH NWP, in which the inset shows an enlarged image taken from the framed region. These results demonstrate that the helical NW inherits the crystallographic structures of the mother pillar in an exact epitaxial way without any detectable mismatch dislocations at the interface even at the atomic scale. We thus conclude that there is no polarity change and the interfacial bonding is the hetero Si−C bonding, as shown in Figure 3e.

Figure 4a shows an SEM image of a BPH NWP, in which the termination point of the pillar (TOP) and that of the helical-wire (TOH) are indicated. Although both finishing ends have sharp tips, TOP is clearly ahead of TOH, which is a clear indication of the mother-daughter relationship. Figure 4b shows the TEM image of another BPH NWP, in which the initiation point of the NWP can be clearly seen. Four diffraction patterns (Figures 4c−f) were taken from four different points: A (alien wire before initiation), B (mother wire), C (initiation point), and D (daughter wire). Except for the single crystalline feature of the alien wire at A, the initiation at C, the daughter wire at D, and the termination point all show well-developed (111) twinning structures, identical to the mother wire at B. This suggests that when the alien wire contacted the mother wire at point C, it immediately became the daughter wire, not only by changing the growth direction but also by copying and inheriting the exact twining structure of the mother wire. Figure 4g−i illustrates how a helical wire would vine grow on the zigzag (mother) pillar. When viewed along [−112] (Figure 4g), the daughter wire shows pseudosingle crystalline atomic structure with no visible kinks (but with small kinks if viewed along ξ directions as shown in Figure S5, Supporting Information). A projected helical angle of 58.5° is revealed. Figure 4h shows a schematic atomic structure model (to be detailed below) viewed in the same direction. The model indicates that the daughter wire speels along [101] whose projection in the [−112] direction, $[101]_P$, has a helical angle of 58.5°. Figure 4i shows the mother−daughter relationship in a two-dimensional unwrapped scheme.

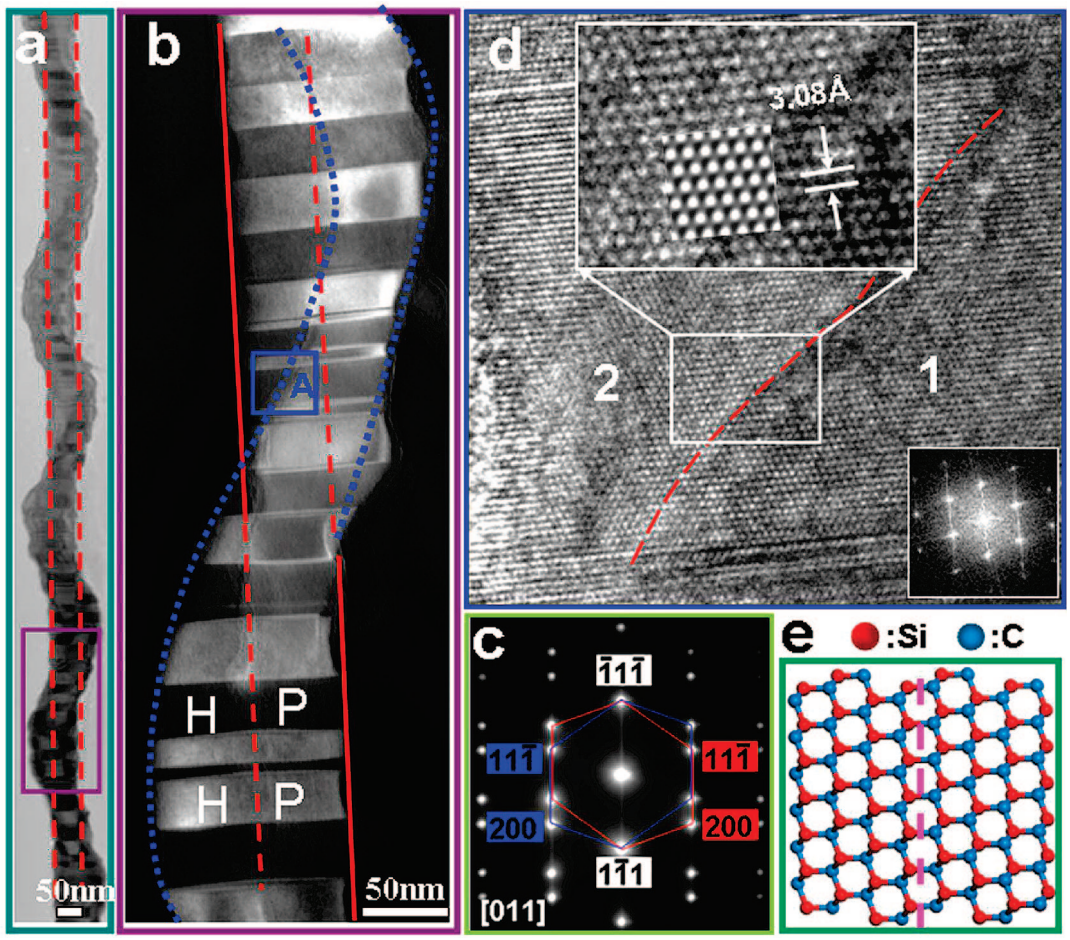

Figure 3. Morphology and the atomic scale structure of the backbone-peripheral-helical NW pair show the near-perfect helical epitaxial feature of the daughter wire with the mother backbone. (a) A typical TEM image of the BPH NWP. (b) An enlarged image of the framed region in (a). Red lines frame the mother (M) pillar whereas blue lines frame the daughter (D) wire, and they show a nearly perfect epitaxial relationship. (c) Selected area electron diffraction pattern (SAEDP) indexed in terms of the [1−11] twinning. (d) High-resolution image to show interfacial structure. An enlarged HRTEM image from the framed region is given in the upper inset. Dynamically simulated HRTEM image (inserted in the same inset) agrees with the HRTEM image. The lower inset shows a fast Fourier transformed pattern confirming single crystalline phase. (e) Atomic model showing hetero Si−C bonding at the BPH interface.

We can understand the formation of the (mother) zigzag pillars in terms of a polar-surface energy difference-driven phenomenon. For zincblende NW grown in the [1−11] polarized direction, the {111} polarized facets (1, 2, 3 and 4 as shown in Figure 1j,k) are the low-energy sidewalls. However, these polarized sidewalls (2, 3 and 4) are not normal to the [1−11] growth direction as shown in Figure 1j,k. This nonorthogonality, and the fact that the polarized energy of the Si-terminated (111), (1−1−1), and (−1−11) side-wall surfaces (surface energy density σ_1) is different from that of the C-terminated (−1−1−1), (−111), and (11−1) side-wall surfaces (surface energy density σ_2), together with the dramatic change of the cross-sectional surface bulky and the cross-sectional polarization energy through the octahedral slab's growth are the primary driving forces for the formation of the superstructural octahedral zigzag pillars and hence for the complex BPH architecture.

To illustrate the point, Figure 5a shows the stacking of two adjacent molecular layers in a cross-sectional view, in which for simplicity each ball represents a SiC molecule. Figure 5b shows the side view. We denote $a = md_{\{110\}}$ and $b = nd_{\{110\}}$ the long and short edges to represent the Si-terminated edges and the carbon-terminated edges in Figure 5a. $d_{\{110\}}$ is the nearest neighboring atomic distance in the polarized {111} plane, and m and n are integers. By using Figure 5a, it is straightforward to show that the long edge a shrinks while the short edge b expands during their growth to be side walls, such that the circumference C of the hexagon is unchanged,

$$3(a+b) = \text{constant } C \quad \text{or} \quad 3d_{\{110\}}(m+n) = C \qquad (1)$$

This implies that $\delta m = -\delta n$. The area of the cross section in Figure 4a is given by

$$S = \frac{1}{2}\cos 30^\circ(a+2b)^2 - 3\frac{1}{2}\cos 30^\circ b^2 = \frac{\sqrt{3}}{4}\left(\frac{C^2}{9} + 2ab\right) \qquad (2)$$

or

$$S = \frac{\sqrt{3}}{4}\left(\frac{C^2}{9} + 2d_{\{110\}}^2 m\cdot n\right) \qquad (2a)$$

The change in S with respect to the change in m, that is, the side-wall surface area, subject to $\delta n = -\delta m$ is thus given by

$$\frac{\delta S}{\delta m} = \frac{\sqrt{3}}{2} d^2_{(110)}(n-m) \quad (3)$$

The cross-sectional area S reaches its maximum when and only when $n = m$, at which the hexagon is equilateral. At this moment, the bulky energy of the cross section of the octahedral nanopillar is the largest. One can show that, at this point, the height of the unit is half of the fully grown octahedral modular unit, namely, $h = h_p/2$ (h_p is the fully grown height of the octahedral slab as shown in Figure S3). On the other hand, the cross-sectional area S also determines the polarization energy difference of the up and bottom surfaces. When and only when the height of the unit reaches fully grown height h_p, the top and bottom surfaces possess a same area and reach an equilibrium condition of the polarization energy.

As the unit in Figure 5a grows, the cross-sectional surface area S increased, and the a edges evolve into the Si-terminated polarized sidewalls, whereas the b edges evolve into the C-terminated polarized sidewalls, with energy density σ_1 and σ_2, respectively (see Figure 5c). For the sake of discussion, here, we assume that the surface polarization energy density $\sigma_2 > \sigma_1$ (to be consistent with the above assumption that $a > b$). Thus, in terms of sidewall energies, the growth of the unit is energetically disfavored because it forces the lower-energy a edges to shrink. In addition, the increase of the cross-sectional surface area S causes a disfavored polarization energy difference to increase (the difference between the top and bottom surface areas increases). However, the increase in surface area S in Figure 5a) translates into an increase in bulk energy when the surface is covered by additional layers to overcome the loss in the sidewall energies and the polarization energy. Further, when a and b edges evolved into side walls, a side-wall bulky energy σ was generated, and it increases with the growth of the octahedral unit. Together with the cross-sectional bulky energy, they are the driving forces for the growth of the {111} octahedral structure unit when the height h is less than $h_p/2$. In other words, so as long as the height h of the unit satisfies $h < h_p/2$, its growth is energetically favored. The situation changes once h exceeds $h_p/2$. Here, not only the increase in the sidewall energy (lower-energy a edges to shrink and higher energy edges to expand) is still energetically disfavored, but also the shrink of the surface area S is also energetically disfavored. The favorable energy comes from two sides: one is still the formed side-wall surface bulky energy σ, and the second one is the polarization energy difference between the up and the bottom surfaces. After reaching the height $h > h_p$, the polarization energy difference between the up and the bottom surfaces decreased and became a driving force to lead the growth of the {111} octahedral unit. Finally, the up and bottom surface polarization-energy difference became to be zero when and only when the top surface area equals to the bottom one, at which,

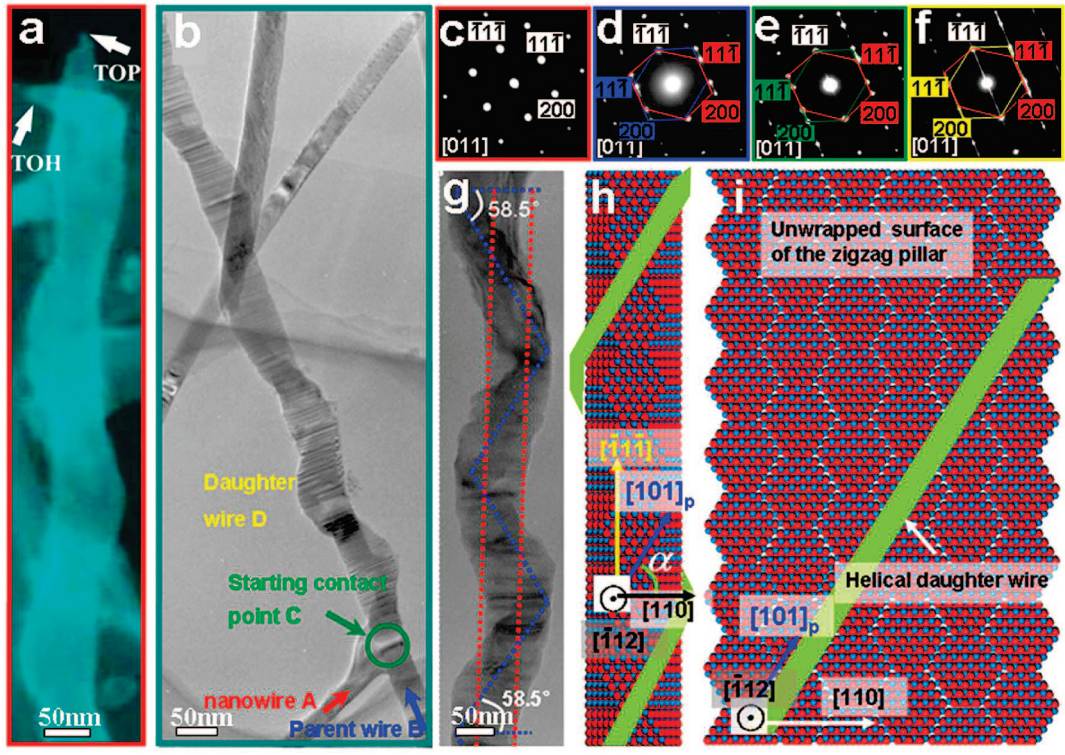

Figure 4. Mother−daughter correlations include the initiation, termination points, and helical features of the BPH NWPs. (a) SEM image of the termination points of a BPH NWP. Both termination points of the mother pillar wire (TOP) and daughter helix wire (TOH) are shown. (b) Another BPH NWP in which the BPH initiation point is readily seen. (c−f) SAEDPs taken at A, alien wire, B, mother wire, C, initiation point, and D, daughter wire in (b), respectively. Through (d−f), the red and green indices are those for matrix and twins, respectively. (g) TEM image of a BPH NWP viewed along [−112]. (h) An atomistic model of (g) showing the daughter wire speeling along $[101]_P$, defined as the [101] axis projected in the viewing direction. (i) The mother−daughter wire relationship unveiled in a two-dimensional unwrapped scheme. Despite that the true helical angle should be 60°, the projected angle here is only 58.5°, as derived in Figure S6.

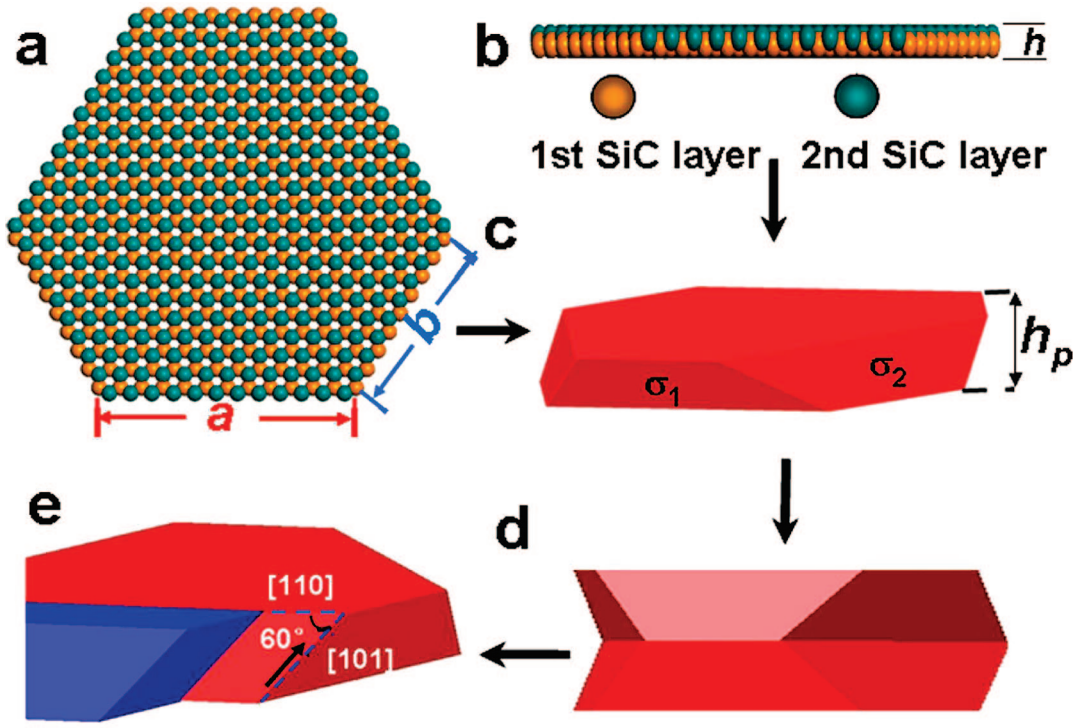

Figure 5. Schematic models show atomic mechanisms forming the superstructural octahedral twinning NWs and the BPH NWPs. (a) Molecular model of the modular unit at its base with only two layers. Letters *a* and *b* denote the long and short edges, respectively. (b) [−112] side view of the model where *h* is the height. (c) A fully grown modular unit of height h_p. (d) Second modular unit on top of the first one with a 60° rotation. (e) Schematic illustration of daughter-wire speeling on mother wire along <110>.

the critical height h_p was reached. At this point, the only favorable energy which can lead the octahedron growth would be side-wall bulky energy. All of the others are energy unfavorable process which includes side-wall energy (lower-energy *a* edges to shrink and higher energy edges to expand), top−bottom surface polarization energy difference, cross-sectional surface area bulky energy. To keep the octahedral unit to continue to grow with the low energy {111} facets, a twin started to form at the growth front in order to terminate the unfavorable growth. This leads to a 60° rotation twin of the next modular unit with respect to the previous one, as shown in Figure 5d. Thus, edge *a* in modular 1 becomes edge *b* in modular 2 and vice versa, so the original energetically favored growth process can be resumed. This leaves behind with the complex pillar architecture in Figure 1l.

From the above discussion, we now understand that the formation of the zigzag pillars is driven by local energetics, not necessarily by global energetics. In other words, these pillars are only kinetically stable. This is because, despite that the {111} surfaces are the lowest-energy surfaces, the zigzag pattern in these pillars increases the surface area considerably with respect to either the hexagonal or the cylindrical pillars as detailed in Figure S3 and Figure S4. Smaller zigzag pillars, with diameter below than 100 nm, have much larger surface areas than hexagonal or cylindrical pillars (10∼20% higher). In addition, the formed zigzag pattern increased a huge amount of sticky cohesion energy which can be as high as several times that of the hexagonal and the cylinder pillars. These global instabilities thus provide high driving forces for the zigzag pillars to attract alien wires to vine grow in order to lower surface energy. This is consistent with our experimental observation that the entire BPH architecture was found only on the zigzag pillars. No helical NW was found on either the popular hexagonal wires or on the cylindrical wires.

The analysis of the experimental helical angles shows a normal distribution with a peak value at about 62° (viewed along [011]) and 58.5° (viewed along [−112]). One can fulfill such angle requirements if the growth of the daughter wires always follow along the [101] edge of the zigzag pillar (Figure 5e). Detailed analyses can be found in Figures S5 and S6. Our analysis further suggests that the daughter wire also possesses the low-energy {111} facets. With such a constraint and that the atomic stacking during the growth must be in the {111} plane, the growth direction of the diameter daughter wire is naturally one of the ξ directions. Upon crossing a twin boundary, the [101] edge of the zigzag pillar rotates by 60° when looking down from [−11−1]. The daughter wire must rotate too. It is energetically favorable for the daughter wire to rotate in the forward direction, as the alternative to rotate backward will crease sharp kinks that are energetically costly.

In summary, our study reveals for the first time covalently bonded SiC BPH NWP and its underlying theoretical mechanisms including local energetics-driven superstructural twinning of the mother wire and inherit chiral growth of the daughter wire. The mechanisms could be universal to other polar materials as well, as octahedral twins, identical to our modular unit, have been observed such as in ZnSe,[29] GaP,[30] InP,[31] ZnS,[32] and others but unexplained.[29−32] More importantly, our essay may initiate a new quest of artificial

materials by using polarity to purposely induce superstructural twins and complex multihierarchical BPH architectures to mimic the functionalities currently present only in bio- and organic systems and to operate at temperature, pressure, and pH value under which such systems simply cannot survive.

Acknowledgment. The work was supported by National Basic Research Program of China (2007CB935400), National 973 program (2002CD613500). X.D.H. was also supported by program for NCET and Beijing NSF/Key Project Funding of Beijing Education Committee (JB102001200801). S.B.Z. was supported by the US DOE/BES.

Supporting Information Available: General morphology; twin planes; dynamic simulation patterns; derivation of the mathematical relationship for the sidewalls; nanowire pillars; calculation of the SZ, SH, and SC; BPH NWP viewed from [110]; zigzag pillar viewed from [112]. This material is available free of charge via the Internet at http://pubs.acs.org.

References

(1) Andrew, H. J. et al. *Nature* **1979**, *282*, 680–686.
(2) Wang, A. J. et al. *Science* **1981**, *211*, 171–176.
(3) Saenger, W. *Principles of Nucleic Acid Structure*; Springer: New York, 1984.
(4) Fukuda, A.; Takanashi, Y.; Isozaki, T.; Ishikawa, K.; Takezoe, H. *J. Mater. Chem.* **1994**, *4*, 997–1016.
(5) Goodby, J. W. *Nature* **1989**, *337*, 449–452.
(6) Green, M. M. *Science* **1995**, *268*, 1860–1866.
(7) Yashima, E.; Maeda, K.; Okamoto, Y. *Nature* **1999**, *399*, 449–451.
(8) Prince, R. B.; Brunsveld, L.; Meijer, E. W.; Moore, J. S. *Angew. Chem., Int. Edit. Engl.* **2000**, *39*, 228–230.
(9) Klepeis, J. L.; et al. *J. Am. Chem. Soc.* **2003**, *125*, 8422–8423.
(10) Rowan, A. E.; Nolte, R. J. M. *Angew. Chem,. Int. Ed. Engl.* **1998**, *37*, 703–706.
(11) Hirschberg, J. H. K.; et al. *Nature* **2000**, *407*, 167–170.
(12) (a) Iijima, S. *Nature* **1991**, *354*, 56–58. (b) Koshio, A.; Yudasaka, M.; Zhang, M.; Iijima, S. *Nano Lett.* **2001**, *1*, 361–363.
(13) (a) Dai, H.; Wong, E. W.; Lu, Y. Z.; Fan, S.; Lieber, C. M. *Nature* **1995**, *375*, 769–772. (b) Wong, E. W.; Sheehan, P. E.; Lieber, C. M. *Science* **1997**, *277*, 1971–1975. (c) Wu, Y.; Cui, Y.; Huynh, L.; Barrelet, C. J.; Bell, D. C.; Lieber, C. M. *Nano Lett.* **2004**, *4*, 433–436.
(14) (a) Zhang, R. Q.; Lifshitz, Y.; Lee, S. T. *Adv. Mater.* **2003**, *15*, 635–640. (b) Hu, J. Q.; Li, Q.; Meng, X. M.; Lee, S. T. *Adv. Mater.* **2002**, *14*, 1396–1399. (c) Kong, Y. C.; Yu, D. P.; Zhang, B.; et al. *Appl. Phys. Lett.* **2001**, *78*, 407–409. (d) Yu, D. P.; et al. *Appl. Phys. Lett.* **1998**, *72*, 3458–3460.
(15) (a) Wang, Z. L.; Gao, R. P.; Gole, J. L.; Stout, J. D. *Adv. Mater.* **2000**, *12*, 1938–1940. (b) Han, X. D.; Zheng, K.; Zhang, Y. F.; Zhang, X. N.; Zhang, Z.; Wang, Z. L. *Adv. Mater.* **2007**, *19*, 2112–2118.
(16) Amelincks, S.; Zhang, X. B.; Bernaerts, D.; Zhang, X. F.; Ivanov, V.; Nagy, J. B. *Science* **1994**, *265*, 635–638.
(17) Zhang, H. F.; Wang, C. M.; Wang, L. S, *Nano Lett.* **2002**, *2*, 941–944.
(18) Zhang, D. Q.; Alkhateeb, A.; Han, H.; Mahmood, H.; McIlroy, D. N.; Norton, M. G. *Nano Lett.* **2003**, *3*, 983–987.
(19) Bell, D. J.; Dong, L. X.; Nelson, B. J.; Golling, M.; Zhang, L.; Grützmacher, D. *Nano Lett.* **2006**, *6*, 725–729.
(20) Kong, X. Y.; Wang, Z. L. *Nano Lett.* **2003**, *3*, 1625–1631.
(21) Yang, R. S.; Ding, Y.; Wang, Z. L. *Nano Lett.* **2004**, *4*, 1309–1312.
(22) Gao, P. X.; et al. *Science* **2005**, *309*, 1700–1704.
(23) Kong, X. Y.; Wang, Z. L. *Appl. Phys. Lett.* **2004**, *84*, 975–977.
(24) Zhang, H. F.; Wang, C. M.; Buck, E. C.; Wang, L. S. *Nano Lett.* **2003**, *3*, 577–580.
(25) (a) Zhou, X. T.; Sham, T. K.; Shan, Y. Y.; Duan, X. F.; Lee, S. T.; Rosenberg, R. A. *J. Appl. Phys.* **2005**, *97*, 104315(1−6). (b) Kim, H. S.; Hwang, S. O.; Myung, Y.; Park, J.; Bae, S. Y.; Ahn, J. P. *Nano Lett.* **2008**, *8*, 551–557.
(26) Bae, S. Y.; Lee, J.; Jung, H.; Park, J.; Ahn, J. P. *J. Am. Chem. Soc.* **2005**, *127*, 10802–10803.
(27) Zhang, L.; et al. *Nano Lett.* **2006**, *6*, 1311–1317.
(28) Tang, Y.; H.; Zhang, Y. F.; Wang, N.; Lee, C. S.; Han, X. D.; Bello, I.; Lee, S. T. *J. Appl. Phys.* **1999**, *85*, 7891–7893.
(29) Li, Q.; Gong, X.; Wang, C.; Wang, J.; Ip, K.; Park, S. *Adv. Mater.* **2004**, *16*, 1436–1440.
(30) Xiong, Q.; Wang, J.; Eklund, P. C. *Nano Lett.* **2006**, *6*, 2736–2742.
(31) Bhunia, S.; Kawamura, T.; Fujikawa, S.; Nakashima, H.; Furukawa, K. *Thin Solid Films* **2004**, *464−465*, 244–247.
(32) Hao, Y. F.; Meng, G. W.; Wang, Z. L.; Ye, C. H.; Zhang, L. D. *Nano Lett.* **2006**, *6*, 1650–1655.
(33) Hao, Y. J.; Jin, G. Q.; Han, X. D.; Guo, X. Y. *Mater. Lett.* **2006**, *60*, 1334–1337.
(34) Spence, J. C. H.; Zuo J. M. *Electron Microdiffraction;* Penum: New York, 1992.

NL080880W